

Research Article

Open Access



Chemical unit co-substitution enabling broadband and tunable near-infrared emission in garnet-type $\text{Lu}_3\text{Sc}_2\text{Ga}_3\text{O}_{12}:\text{Cr}^{3+}$ phosphors

Taoze Wang¹, Gaochao Liu¹, Zhiguo Xia^{1,2}

¹The State Key Laboratory of Luminescent Materials and Devices, Guangdong Provincial Key Laboratory of Fiber Laser Materials and Applied Techniques, School of Materials Science and Engineering, South China University of Technology, Guangzhou 510640, Guangdong, China.

²School of Physics and Optoelectronics, South China University of Technology, Guangzhou 510641, Guangdong, China.

Correspondence to: Dr. Zhiguo Xia, The State Key Laboratory of Luminescent Materials and Devices, South China University of Technology, No. 381, Wushan Road, Guangzhou 510641, Guangdong, China. E-mail: xiazg@scut.edu.cn

How to cite this article: Wang T, Liu G, Xia Z. Chemical unit co-substitution enabling broadband and tunable near-infrared emission in garnet-type $\text{Lu}_3\text{Sc}_2\text{Ga}_3\text{O}_{12}:\text{Cr}^{3+}$ phosphors. *Microstructures* 2022;2:2022020. <https://dx.doi.org/10.20517/microstructures.2022.19>

Received: 1 Aug 2022 **First Decision:** 1 Sep 2022 **Revised:** 24 Sep 2022 **Accepted:** 27 Sep 2022 **Published:** 10 Oct 2022

Academic Editor: Xiaozhou Liao **Copy Editor:** Fangling Lan **Production Editor:** Fangling Lan

Abstract

Although near-infrared phosphor-converted light-emitting diodes (NIR pc-LEDs) are desired for non-visible light source applications, the design of broadband NIR phosphors remains a challenge. Inspired by the chemical unit co-substitution strategy for the modification of composition and local structure, we realize a tunable redshift emission from 706 to 765 nm in garnet-type $\text{Lu}_3\text{Sc}_2\text{Ga}_3\text{O}_{12}:\text{Cr}^{3+}$ with a broadened full width at half maximum and enhanced photoluminescence intensity by introducing a $[\text{Mg}^{2+}-\text{Si}^{4+}]$ unit into the $[\text{Sc}^{3+}-\text{Ga}^{3+}]$ couple. Structural and spectral analyzes demonstrate that the co-substitution reduces the local symmetry and crystal field strength of the $[\text{CrO}_6]$ octahedra, thus leading to inhomogeneous widening of the ${}^4\text{T}_2 \rightarrow {}^4\text{A}_2$ emission and enhanced blue absorption. Furthermore, the ${}^4\text{T}_2 \rightarrow {}^4\text{A}_2$ emission exhibits a phonon-assisted character at low temperatures due to the thermal coupling effect with the ${}^2\text{E}$ level. The fabricated NIR pc-LED based on the optimized NIR phosphor exhibits excellent potential in night vision and imaging applications.

Keywords: Near-infrared (NIR), garnet structure, Cr^{3+} -doped phosphor, co-substitution



© The Author(s) 2022. **Open Access** This article is licensed under a Creative Commons Attribution 4.0 International License (<https://creativecommons.org/licenses/by/4.0/>), which permits unrestricted use, sharing, adaptation, distribution and reproduction in any medium or format, for any purpose, even commercially, as long as you give appropriate credit to the original author(s) and the source, provide a link to the Creative Commons license, and indicate if changes were made.



INTRODUCTION

Broadband near-infrared (NIR, 700–2500 nm) light sources are urgently needed for a variety of applications, including component detection^[1], phototherapy^[1], agricultural plant lighting^[2,3], bioimaging^[4], night vision illumination^[5] and iris recognition^[6]. Among various NIR light sources, however, traditional halogen tungsten lamps suffered from high-power dissipation^[7]. Electroluminescent semiconductors, such as GaAs, are inappropriate for various applications due to their narrow emission band^[8,9]. Furthermore, organic light-emitting diodes (LEDs) suffer from low hydrothermal stability^[10]. In contrast, NIR phosphor-converted (pc)-LEDs that are encapsulated by blue light InGaN chips and NIR-emitting phosphors are emerging as promising candidates to achieve the desired broadband NIR emission. Owing to the commercialization of high-efficiency blue chips^[11,12], the development of NIR phosphors pumped by blue light with broadband and tunable emission has become a research priority^[13].

So far, several types of NIR phosphors have been explored by doping Eu^{2+} ^[14,15], Bi^{16} , Ni^{2+} ^[17], Mn^{4+} ^[18] and Cr^{3+} into inorganic hosts. Among these dopants, Cr^{3+} has gradually become the focus of attention for practical applications due to its high photoluminescence quantum yield^[19–21], broadband and tunable emission^[22,23] and high thermal stability^[24–26]. In addition, the ${}^4\text{A}_2 \rightarrow {}^4\text{T}_1$ transition of Cr^{3+} perfectly matches the blue light chip, as well as a narrowband or tunable broadband emission sensitive to the crystal environment due to the $3d^3$ electronic configuration. Among the different hosts for Cr^{3+} doping, garnet-type compounds possess a compact structure with high symmetry belonging to the cubic system^[27] and have been extensively studied for high-performance NIR phosphors.

The garnet-type structure is composed of three kinds of polyhedra, namely, dodecahedra, mainly occupied by elements with large radii, such as rare earth elements and alkali and alkaline earth metals, octahedra, occupied by transition and main group metals with small radii, and tetrahedra, usually occupied by Ga, Si, Ge, Al, V and P. In recent years, Cr^{3+} -doped garnet phosphors with high internal quantum efficiency (IQE) have been reported and studied. However, owing to the parity-forbidden character of $d-d$ transitions, Cr^{3+} -doped phosphors suffer from a low absorption coefficient (Abs) and narrow emission band. This is particularly true for highly symmetrical lattices, including $\text{Ca}_3\text{Sc}_2\text{Si}_3\text{O}_{12}:\text{Cr}^{3+}$ (IQE/Abs = 92.3%/27.6%, FWHM = 110 nm)^[28] and $\text{Gd}_3\text{Sc}_2\text{Ga}_3\text{O}_{12}:\text{Cr}^{3+}$ (IQE/Abs = 98.6%/21.0%, FWHM = 120 nm)^[29], which limits the further application of NIR pc-LEDs. Although the Abs can be raised by increasing the concentration of Cr^{3+} , excessive dopants usually lead to serious concentration quenching effects and stronger electron-phonon coupling, resulting in damage to the thermal stability and IQE in the garnet structure^[30,31]. Although Cr^{3+} and Yb^{3+} co-doping may benefit the broadening emission spectrum and enhance the thermal stability, it has little effect on improving the Abs^[32]. It has been reported that introducing the odd-parity crystal field by lattice distortion can partly release the parity-forbidden character of Cr^{3+} ions so that an improved Abs is expected^[33].

In recent years, the chemical unit co-substitution strategy, i.e., the simultaneous substitution of two kinds of chemical units in a crystal structure, has been used to realize structural evolution and the regulation of luminescence properties, as proposed by our group and successfully adopted by many different research teams^[34]. Benefitting from the high structural tolerance of the garnet structure, chemical units can enter the cell in large quantities to realize the distortion of the polyhedra and the disorder of the local crystal environment, further breaking the reverse symmetry of the crystal site, where Cr^{3+} is located. Thus it leads to a strong crystal field splitting and contributes to the photoluminescence tuning of the emission band.

In this work, an enhanced NIR emission of Cr^{3+} ions with a broadened FWHM is realized by co-substituting $[\text{Mg}^{2+}-\text{Si}^{4+}]$ for $[\text{Sc}^{3+}-\text{Ga}^{3+}]$ in garnet-type $\text{Lu}_3\text{Sc}_{1.98-x}\text{Mg}_x\text{Ga}_{3-x}\text{Si}_x\text{O}_{12}:0.02\text{Cr}^{3+}$ phosphors. The luminescence

properties and crystal field strength of the phosphors are further studied as a function of x . We find that the thermal coupling effect of the 4T_2 and 2E levels and the electron-phonon coupling effect are enhanced with increasing x and the related luminescence mechanism is proposed. Finally, a broadband NIR pc-LED is designed and fabricated using the composition-optimized phosphor $\text{Lu}_3\text{Sc}_{1.38}\text{Mg}_{0.6}\text{Ga}_{2.4}\text{Si}_{0.6}\text{O}_{12}:0.02\text{Cr}^{3+}$ (LSMGS:Cr) and its applications in imaging and night vision illuminating are demonstrated.

MATERIALS AND METHODS

Materials and preparation

The $\text{Lu}_3\text{Sc}_{1.98-x}\text{Mg}_x\text{Ga}_{3-x}\text{Si}_x\text{O}_{12}:0.02\text{Cr}^{3+}$ samples ($x = 0.0, 0.30, 0.45, 0.60, 0.75$ or 0.90) were prepared by a conventional high-temperature solid-state method. Lu_2O_3 (99.9%, Aladdin), Sc_2O_3 (99.9%, Aladdin), MgO (99.9%, Aladdin), Ga_2O_3 (99.99%, Aladdin), SiO_2 (99.99%, Macklin) and Cr_2O_3 (99.95%, Aladdin) were used as the starting materials and weighed according to stoichiometric proportions, with 2 wt.% H_3BO_3 (99.5%, Aladdin) added as the flux. After being mixed and grounded thoroughly using ethanol in an agate mortar, the mixtures were transferred into alumina crucibles (Kaiping Shengxing Chemical Porcelain Factory, Tangshan, 16×28 mm) and then placed in a box furnace for sintering at 1450°C for 6 h in air. Finally, the phosphors were ground in an agate mortar for 3 min after cooling to room temperature.

Characterization

Powder X-ray diffraction patterns were measured using a diffractometer (PANalytical Corporation, Netherlands) with a $\text{Cu K}\alpha$ radiation source ($\lambda = 1.5406 \text{ \AA}$) and the operating voltage and current set as 40 kV and 15 mA, respectively. Room-temperature photoluminescence (PL) and photoluminescence excitation (PLE) spectra were recorded using an FLS1000 fluorescence spectrophotometer (Edinburgh Instruments, UK) equipped with a continuous xenon lamp (450 W) as the excitation source and a liquid-nitrogen cooled NIR photomultiplier tube as the detector (Hamamatsu, R5509, InP/InGaAsP). Low-temperature spectra were measured using the same spectrophotometer equipped with a Cryo-77 low-temperature fluorescence instrument (Tian Jin Orient - KOJI Instrument Co., Ltd.). The PL decay curve was also measured using the same spectrophotometer with a microsecond flash lamp (μF900) as the excitation source. High-temperature spectra were measured by a fiber spectrophotometer (NOVA high-sensitivity spectrometer, Idea Optics, China) equipped with a TAP-02 high-temperature fluorescence instrument (Tian Jin Orient - KOJI Instrument Co., Ltd.) and a 450 nm laser diode as the excitation source. Diffuse reflection (DR) spectra were collected using a UV-Vis-NIR spectrophotometer (Hitachi UH4150) and BaSO_4 was used as the reference standard. The quantum efficiency at room temperature was measured by an absolute PL quantum yield spectrometer (Quantaury-QY Plus C13534-12, Hamamatsu Photonics).

LED device fabrication and performance measurements

The pc-NIR LED device was designed and made by coating the as-prepared phosphor on a blue LED (X1901, 5 W, Guangzhou LEDteen Optoelectronics Co., Ltd., China) and fully blending with an epoxy resin. The electroluminescence of the fabricated NIR pc-LED was measured by Optical & Electrical Fast Meters For LEDS (Hangzhou Hopoo Optoelectronics Technology Co., Ltd., China).

RESULTS AND DISCUSSION

Crystal structure of $\text{Lu}_3(\text{Sc}, \text{Mg})_2(\text{Ga}, \text{Si})_3\text{O}_{12}:\text{Cr}^{3+}$

The phase and purity of the as-prepared powder samples were examined by X-ray diffraction and the results are shown in [Figure 1A](#). The x value reflects the degree of co-substitution of $[\text{Mg}^{2+}\text{-Si}^{4+}]$ for $[\text{Sc}^{3+}\text{-Ga}^{3+}]$. All diffraction peaks were well matched with the standard data of the $\text{Lu}_3\text{Sc}_2\text{Ga}_3\text{O}_{12}$ cubic phase (PDF No. 54-1252, space group $Ia-3d$) and no obvious impurity phases were observed, indicating that the phase of the samples was not affected by a certain amount of chemical unit co-substitution due to the high structural tolerance of garnet-type compounds as shown in [Figure 1C](#).

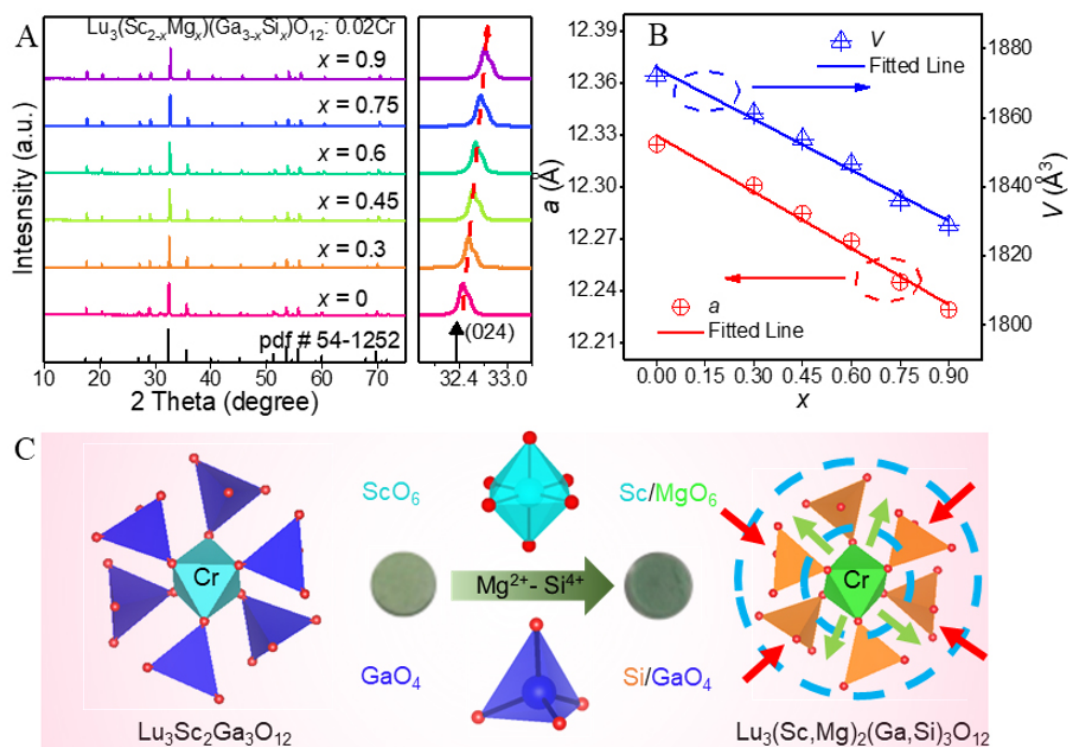


Figure 1. (A) XRD patterns of $\text{Lu}_3\text{Sc}_{1.98-x}\text{Mg}_x\text{Ga}_{3-x}\text{Si}_x\text{O}_{12}:0.02\text{Cr}^{3+}$ ($x = 0.0-0.9$) with selected diffraction peak near 32.7° . (B) Calculated lattice parameters of $\text{Lu}_3\text{Sc}_{1.98-x}\text{Mg}_x\text{Ga}_{3-x}\text{Si}_x\text{O}_{12}:0.02\text{Cr}^{3+}$ ($x = 0.0-0.9$). (C) Crystal structure of $\text{Lu}_3\text{Sc}_{1.98-x}\text{Mg}_x\text{Ga}_{3-x}\text{Si}_x\text{O}_{12}:0.02\text{Cr}^{3+}$.

The shift of the strongest diffraction peak to a higher angle, as shown in Figure 1A, indicates that the cell shrinks with increasing x . With the substitution of $[\text{Mg}^{2+}\text{-Si}^{4+}]$ for $[\text{Sc}^{3+}\text{-Ga}^{3+}]$, the diffraction peak near 32.7° shifts slightly toward a higher angle [Figure 1A] due to the ionic radii of Mg^{2+} [0.72 Å, coordination number (CN) = 6] and Si^{4+} (0.26 Å, CN = 4) being smaller than that of Sc^{3+} (0.745 Å, CN = 6) and Ga^{3+} (0.47 Å, CN = 4), respectively^[35]. The lattice parameter of the phosphors in the cubic system was calculated using the Bragg equation:

$$2d \sin\theta = \lambda \quad (1)$$

$$\frac{1}{d^2} = \frac{h^2 + k^2 + l^2}{a^2} \quad (2)$$

where d and a represent the interplanar spacing and lattice parameter, respectively. The wavelength of the incidence X-ray λ was 1.5406 Å. The diffraction peak position θ originating from the crystal face (hkl) was obtained from the strongest diffraction peak near 32.7° in Figure 1A, where h , k and l are the Miller indices, namely, 0, 2 and 4, respectively, in the calculation. The lattice parameter decreased from 12.32 to 12.23 Å with increasing x , as shown in Figure 1B. This indicates that the $[\text{Mg}^{2+}\text{-Si}^{4+}]$ chemical unit had been successfully incorporated into the garnet-type structure. The shrinkage of the crystal cell usually enhances the crystal field strength of the octahedrally-coordinated Cr^{3+} center with a blueshift and narrowed emission band. In contrast, a completely opposite phenomenon in $\text{Lu}_3\text{Sc}_2\text{Ga}_3\text{O}_{12}:\text{Cr}^{3+}$ can be observed after the $[\text{Mg}^{2+}\text{-Si}^{4+}]$ chemical unit was introduced, as discussed below.

Photoluminescence properties of $\text{Lu}_3(\text{Sc, Mg})_2(\text{Ga, Si})\text{O}_{12}:\text{Cr}^{3+}$

The room-temperature emission (PL) and excitation (PLE) spectra of $\text{Lu}_3\text{Sc}_{1.98}\text{Ga}_3\text{O}_{12}:\text{0.02Cr}^{3+}$ are shown in [Figure 2A](#). Under the excitation of 440 nm blue light, $\text{Lu}_3\text{Sc}_{1.98}\text{Ga}_3\text{O}_{12}:\text{0.02Cr}^{3+}$ exhibits a dark-red emission with a FWHM of 88 nm centered at 706 nm, which is attributed to the ${}^2\text{E} \rightarrow {}^4\text{A}_{2g}$ transition of Cr^{3+} . When monitored at the 706 nm emission, $\text{Lu}_3\text{Sc}_{1.98}\text{Ga}_3\text{O}_{12}:\text{0.02Cr}^{3+}$ gave three excitation bands in the UV, blue and red regions, which were assigned to the ${}^4\text{A}_2 \rightarrow {}^4\text{T}_1$ (${}^4\text{P}$), ${}^4\text{A}_2 \rightarrow {}^4\text{T}_1$ (${}^4\text{F}$) and ${}^4\text{A}_2 \rightarrow {}^4\text{T}_2$ (${}^4\text{F}$) transitions of Cr^{3+} , respectively. After the $[\text{Mg}^{2+}\text{-Si}^{4+}]$ unit replaces the $[\text{Sc}^{3+}\text{-Ga}^{3+}]$ couple in the structure, the emission band position gradually shifts from 706 to 765 nm. Furthermore, the FWHM is doubled to 176 nm [[Figure 2B](#)]. The $\text{Lu}_3\text{Sc}_{1.38}\text{Mg}_{0.6}\text{Ga}_{2.4}\text{Si}_{0.6}\text{O}_{12}:\text{0.02Cr}^{3+}$ phosphor has a broadband NIR emission with stronger penetrability and crypticity, which is more conducive to its application in biological imaging and component analysis compared to $\text{Lu}_3\text{Sc}_{1.98}\text{Ga}_3\text{O}_{12}:\text{0.02Cr}^{3+}$ with a narrowband visible dark-red emission.

The change in the spectrum can be divided into two stages, as shown in [Figure 2C](#). In the first stage ($x = 0.0\text{-}0.45$), the emission band position rapidly redshifts and the FWHM increases significantly, mainly as a result of the enhancement of the broadband ${}^4\text{T}_2 \rightarrow {}^4\text{A}_2$ emission, indicating that the excited electrons gradually tend to populate at the ${}^4\text{T}_2$ state rather than the ${}^2\text{E}$ state. The enhancement of the parity-forbidden ${}^4\text{T}_2 \rightarrow {}^4\text{A}_2$ transition is a common phenomenon in garnet oxide solid solutions^[36] and is usually caused by the disordered local crystal environment of Cr^{3+} due to the introduction of the chemical unit. In the second stage ($x = 0.6\text{-}0.9$), the values of the emission band position and FWHM increased slowly and finally converged to a constant. This may be caused by two competing factors. The first is the crystal field enhancement caused by the lattice contraction discussed previously, which usually engenders the blueshift and sharpens the Cr^{3+} emission. The second factor is the disordered local crystal environment, which usually engenders the redshift and broadens the Cr^{3+} emission.

Because of the lack of protection from an external shell, the orbital energy levels of the d orbital of Cr^{3+} are very sensitive to the influence of the host lattice. Therefore, to explore the further influence of the $[\text{Mg}^{2+}\text{-Si}^{4+}]$ chemical unit substitution on the emission properties of Cr^{3+} , it is necessary to quantitatively calculate the crystal field splitting parameters, including Dq , B and C . According to crystal field theory, the crystal field strength parameter Dq and Racah parameter B can be approximated by the following equations^[37]:

$$10Dq = E({}^4\text{T}_{2g}) \quad (3)$$

$$\frac{Dq}{B} = \frac{15(\Delta E / Dq - 8)}{(\Delta E / Dq)^2 - 10(\Delta E / Dq)} \quad (4)$$

$$\Delta E = E({}^4\text{T}_{1g}) - E({}^4\text{T}_{2g}) \quad (5)$$

Finally, the Racah parameter C can be calculated by:

$$E({}^2\text{E}) = 3.05C + 7.9B - 1.8B^2 / Dq \quad (6)$$

where $E({}^4\text{T}_{1g})$ and $E({}^4\text{T}_{2g})$ are the energy levels of ${}^4\text{T}_{1g}({}^4\text{F})$ and ${}^4\text{T}_{2g}({}^4\text{F})$ for Cr^{3+} , respectively, which can be obtained from the PLE spectra, and $E({}^2\text{E})$ is the equilibrium position of the sharp zero-photon line (ZPL) obtained from the PL spectra.

The Racah parameter B represents the repulsion between electrons in the $3d$ orbital of Cr^{3+} . The value of the Racah parameter B of Cr^{3+} in the host is usually lower than in the free environment ($B_0 = 918 \text{ cm}^{-1}$) and

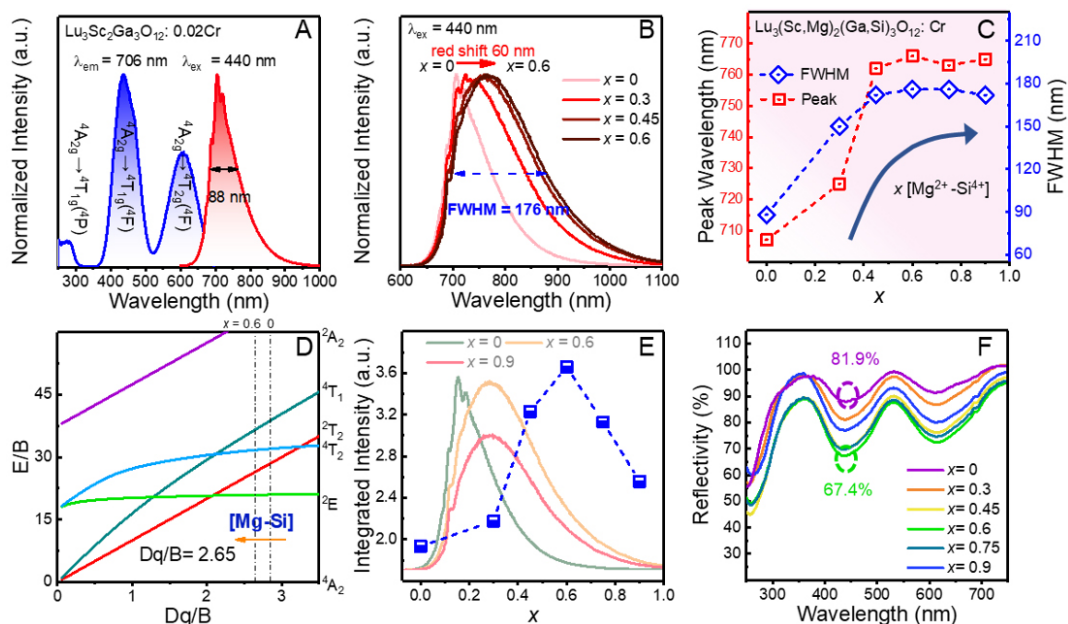


Figure 2. (A) Room-temperature PLE (blue) and PL (red) spectra of $\text{Lu}_3\text{Sc}_{1.98}\text{Ga}_3\text{O}_{12}:0.02\text{Cr}^{3+}$ phosphor. (B) Normalized PL spectra of $\text{Lu}_3\text{Sc}_{1.98-x}\text{Mg}_x\text{Ga}_3\text{Si}_x\text{O}_{12}:0.02\text{Cr}^{3+}$ ($x = 0.0-0.6$) excited by 440 nm light. (C) Peak wavelength and FWHM of $\text{Lu}_3\text{Sc}_{1.98-x}\text{Mg}_x\text{Ga}_3\text{Si}_x\text{O}_{12}:0.02\text{Cr}^{3+}$ ($x = 0.0-0.9$). (D) Tanabe-Sugano diagram of Cr^{3+} in the perfect octahedral environment. (E) Integrated intensity of PL spectra of $\text{Lu}_3\text{Sc}_{1.98-x}\text{Mg}_x\text{Ga}_3\text{Si}_x\text{O}_{12}:0.02\text{Cr}^{3+}$ ($x = 0.0-0.9$) excited by 440 nm light. (F) DR spectra of $\text{Lu}_3\text{Sc}_{1.98-x}\text{Mg}_x\text{Ga}_3\text{Si}_x\text{O}_{12}:0.02\text{Cr}^{3+}$ ($x = 0.0-0.9$).

strongly depends on the covalency of the host. Accordingly, the specific crystal field parameters of $\text{Lu}_3\text{Sc}_{1.98-x}\text{Mg}_x\text{Ga}_3\text{Si}_x\text{O}_{12}:0.02\text{Cr}^{3+}$ ($x = 0.0, 0.6$ or 0.9) were calculated, as listed in Table 1. The value of Dq/B decreases from 2.85 to 2.65 with increasing x value, thus reducing the energy separation between ${}^4\text{T}_{2g}$ and ${}^2\text{E}$ [Figure 2D]. The decreased B values indicate that the ionic character of the octahedra in which Cr^{3+} is located is enhanced due to the enlargement of the $[\text{Sc}/\text{MgO}_6]$ octahedra, even though the whole crystal cell shrinks under co-substitution^[38]. Therefore, the excited electrons will tend to reside in the gradually redshifted ${}^4\text{T}_{2g}$ level due to the weakening crystal field and induction of a broad NIR emission (${}^4\text{T}_2 \rightarrow {}^4\text{A}_2$). As shown in Figure 2E, with increasing x , the integral intensity of $\text{Lu}_3\text{Sc}_{1.98-x}\text{Mg}_x\text{Ga}_3\text{Si}_x\text{O}_{12}:0.02\text{Cr}^{3+}$ increased to 180% of the original value at first ($x = 0.0-0.6$) and then decreased ($x = 0.6-0.9$). Figure 2F shows the DR spectra of the $\text{Lu}_3\text{Sc}_{1.98-x}\text{Mg}_x\text{Ga}_3\text{Si}_x\text{O}_{12}:0.02\text{Cr}^{3+}$ series. The three absorption bands of Cr^{3+} in the UV-Vis region fit well with the three excitation bands of the PLE spectra. With the introduction of $[\text{Mg}^{2+}\text{-Si}^{4+}]$ chemical units in the structure ($x = 0.0-0.6$), the reflectance at 440 nm reduces from 81.9% for $x = 0.0$ to 67.4% for $x = 0.6$, which indicates that more blue light was absorbed by the optimized phosphor.

The external quantum efficiency (EQE) of the designed phosphors is crucial for high-performance NIR LEDs and is the product of the internal quantum efficiency (IQE) and Abs^[39,40]. The quantum yield of the samples was measured and the values of the EQE, IQE and Abs are shown in Figure 3A. The matrix garnet phosphor ($x = 0.0$) shows a high IQE of up to 81.4% and a low Abs (0.257) due to the parity-forbidden transition of Cr^{3+} . The $[\text{Mg}^{2+}\text{-Si}^{4+}]$ co-substituted phosphor ($x = 0.6$) demonstrated a higher EQE (28.1%) compared to the matrix phosphor (20.9%) on account of the improvement of the absorption ability from 25.7% (light green body color) to 38.4% (deep green body color). Excessive $[\text{Mg}^{2+}\text{-Si}^{4+}]$ chemical units were harmful to the luminescence ability of the $\text{Lu}_3\text{Sc}_{1.98-x}\text{Mg}_x\text{Ga}_3\text{Si}_x\text{O}_{12}:0.02\text{Cr}^{3+}$ phosphors ($x = 0.75$ or 0.90), which is consistent with the trend of the integral intensity of the PL spectra [Figure 2E]. The decreased trend of the Abs of $\text{Lu}_3\text{Sc}_{1.98-x}\text{Mg}_x\text{Ga}_3\text{Si}_x\text{O}_{12}:0.02\text{Cr}^{3+}$ phosphors ($x = 0.75$ or 0.90) may be caused by more

Table 1. Crystal field parameters of $\text{Lu}_3\text{Sc}_{1.98-x}\text{Mg}_x\text{Ga}_3\text{Si}_x\text{O}_{12}:0.02\text{Cr}^{3+}$ ($x = 0.0, 0.6$ or 0.9) phosphors

Host	Dq (cm^{-1})	B (cm^{-1})	Dq/B	C (cm^{-1})
$x = 0$	1514	531	2.85	3499
$x = 0.6$	1463	553	2.65	3445
$x = 0.9$	1460	556	2.62	3415

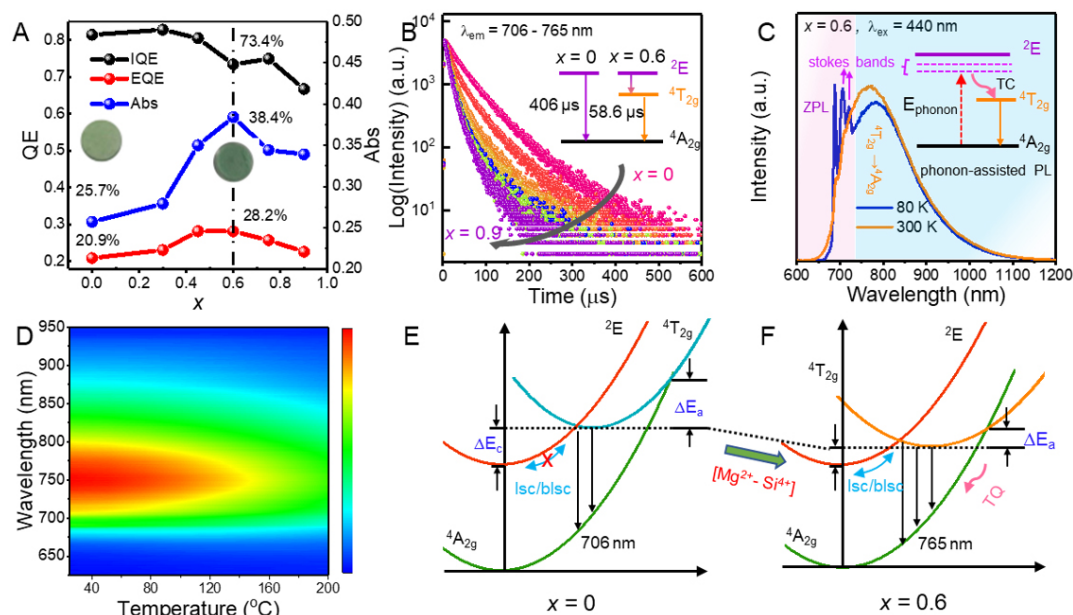


Figure 3. (A) IQE, Abs and EQE values of $\text{Lu}_3\text{Sc}_{1.98-x}\text{Mg}_x\text{Ga}_3\text{Si}_x\text{O}_{12}:0.02\text{Cr}^{3+}$ phosphors. (B) Luminescence decay curves of $\text{Lu}_3\text{Sc}_{1.98-x}\text{Mg}_x\text{Ga}_3\text{Si}_x\text{O}_{12}:0.02\text{Cr}^{3+}$ phosphors ($x = 0.0-0.9$) excited by 440 nm light and monitored at their strongest emission wavelength. (C) Temperature-dependent PL spectra and phonon-assisted PL mechanism of LSMGS:Cr excited by 440 nm light at 80 and 300 K. (D) PL/temperature correlation maps of LSMGS:Cr excited by 440 nm light. (E) and (F) Configuration coordinate diagrams of $\text{Lu}_3\text{Sc}_{1.98-x}\text{Mg}_x\text{Ga}_3\text{Si}_x\text{O}_{12}:0.02\text{Cr}^{3+}$ ($x = 0.0$ or 0.6) showing level thermal coupling and temperature-quenching mechanisms.

serious diffuse reflection due to the mismatched refractive index between the garnet phase and the impurities.

The experiment results show that the PL decay curves can only be fitted with a bi-exponential function [Figure 3B]:

$$I(t) = A_1 e^{-\frac{t}{\tau_1}} + A_2 e^{-\frac{t}{\tau_2}} \quad (7)$$

where $I(t)$ represents the emission intensity at a certain time t , A_1 and A_2 are constants and τ_1 and τ_2 are the luminescence decay times. According to the above equation, the decay times were determined to be 406.1, 218.4 and 195.3 μs for τ_1 and 185.1, 58.6 and 56.0 μs for τ_2 , corresponding to the $x = 0.0, 0.6$ or 0.9 samples, respectively. It is known that Cr^{3+} generally exists stably at octahedral sites. Although Cr^{3+} will occupy both octahedral and dodecahedral sites in some garnet oxides, the PL band of Cr^{3+} at dodecahedral sites usually exhibits longwave PL (> 800 nm) due to the larger radius of the polyhedra^[31]. Thus, the bi-exponential PL decay was more likely caused by one crystallographic site with multiple local crystal environments.

The two lifetimes with different orders can be attributed to the ${}^2E \rightarrow {}^4A_{2g}$ and ${}^4T_{2g} \rightarrow {}^4A_{2g}$ transition, respectively. The ${}^2E \rightarrow {}^4A_{2g}$ transition is both parity-forbidden and spin-forbidden, while the ${}^4T_{2g} \rightarrow {}^4A_{2g}$ transition is parity-forbidden but spin-allowed, which causes the former to have a longer lifetime. The transition from the 2E state becomes partially allowed due to the overlap between the wavefunctions of the 2E and 4T_2 states, which explains the shorter decay time in the phosphors after co-substitution. This phenomenon suggests that the excited electrons are populated at both the 2E and ${}^4T_{2g}$ levels, which further indicates that Cr^{3+} in $Lu_3Sc_{1.98-x}Mg_xGa_{3-x}Si_xO_{12}$ may possess more than one set of Dq/B values, which also explains why the total crystal field strength calculated in Figure 2D was not at a medium level and the inhomogeneous broadening in the PL spectra. The bi-exponential decay of the matrix may be caused by anti-site defects, which were previously reported in $Lu_3Sc_2Ga_3O_{12}:Cr^{3+}$ [41]. Overall, co-substitution will induce a local structural distortion and then introduce sites with weaker crystal field strength, as well as the partial lifting of the forbidden ${}^4T_{2g} \rightarrow {}^4A_{2g}$ transition due to the high symmetry. The phenomenon where two luminescence components in the inhomogeneous broadening PL spectra can be detected when monitored at a certain wavelength, indicating the nonnegligible thermal coupling of the 2E and ${}^4T_{2g}$ levels, as discussed below. The PL lifetimes decreased with increasing x [Supplementary Figure 1] due to the partial lifting of the restriction on the forbidden transition and the increase in the probability of the non-radiative transition.

To investigate the detailed luminescence mechanism herein, the low-temperature-dependent PL spectra and PL decay curves of LSMGS:Cr were recorded and compared in Figure 3C, Supplementary Figures 2 and 3. At 80 K, the PL spectra of LSMGS:Cr consist of a sharp ZPL, namely, the ${}^2E \rightarrow {}^4A_{2g}$ transition at 690 nm and the attached Stokes sideband (705 and 720 nm) due to the participation of phonons. The ${}^4T_{2g} \rightarrow {}^4A_{2g}$ transition presented as a broadband emission centered at 785 nm. With increasing temperature, the intensity of the ${}^2E \rightarrow {}^4A_{2g}/{}^4T_{2g} \rightarrow {}^4A_{2g}$ transition enhanced at first and then decreased significantly when the temperature exceeded 125 K. This similar phenomenon related to the ZPL and Stokes sideband also exists in other transition metal-doped phosphors with the $3d^3$ electronic configuration, such as V^{2+} and Mn^{4+} [42,43]. The dopants in the host introduce point defects, which can accept energy from not only photons but also phonons in the host lattice to produce luminescence. The latter, known as phonon-assisted emission, will be enhanced by more phonons according to the Bose-Einstein distribution law when heating from a low temperature. When the temperature is raised to a specific level, the large number of phonons induces serious electron-phonon coupling, which leads to thermal quenching.

The ${}^4T_{2g} \rightarrow {}^4A_{2g}$ emission with the same behavior was abnormal compared to other Cr-doped phosphors. Generally, phosphors at low temperatures exhibit a stronger emission because the lattice vibration is inhibited, which weakens the electron-phonon coupling effect and causes a smaller probability of non-radiative transition. The abnormal ${}^4T_{2g} \rightarrow {}^4A_{2g}$ PL behavior related to the temperature indicates that the thermal coupling effect between the 2E and ${}^4T_{2g}$ levels did exist in $Lu_3Sc_{1.98-x}Mg_xGa_{3-x}Si_xO_{12}:0.02Cr^{3+}$ so that the phonon energy can transfer between these two levels by back-intersystem crossing/intersystem crossing (blsc/lsc)[44]. The phonon-assisted emission was also present in the solid solution with $x = 0.45$, as shown in Supplementary Figure 4. In addition, the PL decay also can be fitted with a bi-exponential function with a reduced lifetime compared with that at 80 K due to the increasing portion of ${}^4T_{2g} \rightarrow {}^4A_{2g}$ emission during the blsc process and more serious electron-phonon coupling. In the Cr-doped phosphor, weakening of the crystal field strength caused by lattice thermal expansion with increasing temperature leads to a redshift in the PL spectra. In LSMGS:Cr, however, the emission center with a larger Stokes shift will suffer more serious thermal quenching, resulting in the 20 nm blueshift of the emission spectrum at high temperature, which is common in disordered local crystal environment, such as Cr-doped glasses[45], which further proves the disorder of the local structure in LSMGS:Cr. Even though the non-radiative transition to some extent exists in the LSMGS:Cr, it still retains 75% at 423 K of the initial intensity measured at room temperature

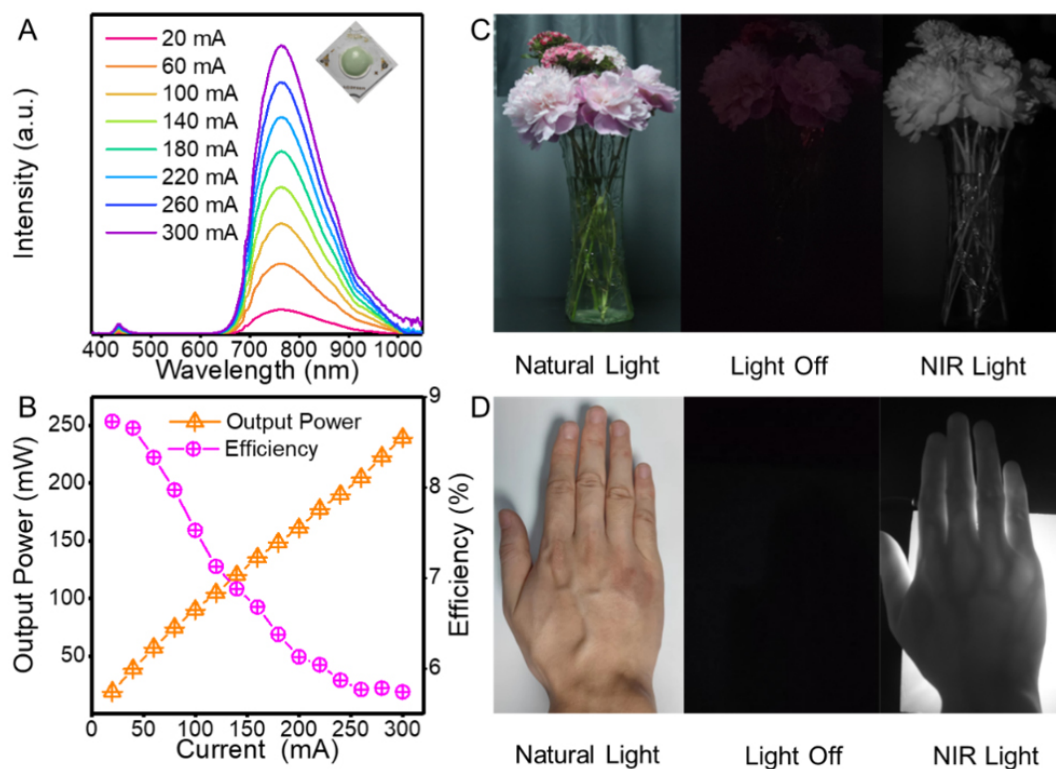


Figure 4. (A) Photograph and luminescence spectra of as-fabricated NIR pc-LED. (B) NIR output power and photoelectric efficiency of pc-LED measured at current from 20 to 300 mA. (C) Photographs of bouquet under natural and NIR light captured by different cameras. (D) Photographs of NIR light transilluminating human palm.

and maintains fine color stability [Figure 3D and Supplementary Figure 5], which benefits from the high structural rigidity of the garnet.

In summary, the mechanism of $[\text{Mg}^{2+}\text{-Si}^{4+}]$ co-substitution on the regulation of optical properties can be qualitatively explained, as shown in Figure 3E and F. The $[\text{Mg}^{2+}\text{-Si}^{4+}]$ chemical units not only introduce more multiple local crystal environments but also reduce the energy level gap ΔE_c between ${}^4\text{T}_{2g}$ and ${}^2\text{E}$, which is closely related to the crystal field strength. Thus, the energy level thermal coupling enhances, which allows part of the excited electrons at the ${}^2\text{E}$ level can also populate into the ${}^4\text{T}_{2g}$ level through the back-intersystem crossing process with increasing x and eventually leads to the transition from a short wavelength sharp emission to a long wavelength broad emission. However, the weak crystal field strength simultaneously causes the reduction of the thermal activation barrier ΔE_a , which causes more serious electron-phonon coupling and thermal quenching, thereby weakening the luminescence performance, which is consistent with the results of the luminescence analysis and thermal stability [Figures 2E and 3A; Supplementary Figure 6].

Application in a NIR pc-LED

To demonstrate the potential application of NIR pc-LEDs in night vision illumination and the penetrating imaging of biological tissue, a broadband NIR pc-LED device was designed and fabricated using the LSMGS:Cr ($x = 0.6$) phosphor on a blue light-emitting InGaN chip (440 nm), as shown in Figure 4A. The NIR output power continuously increases with the drive current and reaches 90.3 mW at 100 mA. Furthermore, the photoelectric efficiency of pc-LED drops from 8.73% to 5.74% due to the efficiency drop of LED chips, as shown in Figure 4B. Figure 4C shows that a bouquet can be vividly captured by a NIR camera

using a 720 nm long-pass filter under the non-visible illumination of the NIR pc-LED, which shows the feasibility of its application in night vision. The veins of a human palm can be distinguished, as shown in [Figure 4D](#), using NIR light to penetrate and a NIR camera to capture, because NIR light has a good penetrability through biological tissue and veins have a specific absorption of NIR light. This fundamental demonstration indicates that the LSMGS:Cr phosphors can be potentially applied in machine vision and non-destructive examination.

CONCLUSIONS

Broadband NIR phosphors $\text{Lu}_3\text{Sc}_{1.98-x}\text{Mg}_x\text{Ga}_{3-x}\text{Si}_x\text{O}_{12}:0.02\text{Cr}^{3+}$ ($x = 0.0-0.9$) with tunable emission were successfully fabricated by a high-temperature solid-state method. The shrinkage of the crystal cell and pure phase were verified by XRD analysis. By co-substituting $[\text{Sc}^{3+}\text{-Ga}^{3+}]$ with $[\text{Mg}^{2+}\text{-Si}^{4+}]$ chemical units in the garnet host with high symmetry, the $[\text{CrO}_6]$ octahedra were distorted, thus breaking the inversion symmetry and leading to the broadband ${}^4\text{T}_2 \rightarrow {}^4\text{A}_2$ emission. Furthermore, the $[\text{Mg}^{2+}\text{-Si}^{4+}]$ pairs strengthened the thermal coupling between the ${}^4\text{T}_2$ and ${}^2\text{E}$ levels due to the weakened crystal field strength, resulting in both sharp ZPL and broad emissions. Under 440 nm blue light excitation, the composition-optimized garnet-type solid solution demonstrated an inhomogeneous widening NIR emission maximized at 765 nm, with a large FWHM of 176 nm and highest EQE/Abs of 28.2%/38.4% for the composition of $x = 0.6$ ($\text{Lu}_3\text{Sc}_{1.38}\text{Mg}_{0.6}\text{Ga}_{2.4}\text{Si}_{0.6}\text{O}_{12}:0.02\text{Cr}^{3+}$). The fabricated broadband NIR pc-LED showed a light outpower of 90.3 mW at 100 mA with a photoelectric efficiency of 7.5%, demonstrating its application potential in multiple fields.

DECLARATIONS

Authors' contributions

Conceived and drafted the manuscript: Xia Z, Wang T

Prepared material and device, performed characterization: Wang T

Performed data analysis: Wang T, Liu G

Revised the manuscript: Xia Z

Availability of data and materials

The data that support the findings of this study are available from the corresponding author upon reasonable request.

Financial support and sponsorship

The work was supported by International Cooperation Project of National Key Research and Development Program of China (2021YFB3500400 and 2021YFE0105700), the National Natural Science Foundations of China (Grant Nos. 51972118), Guangzhou Science & Technology Project (202007020005), and the Local Innovative and Research Teams Project of Guangdong Pearl River Talents Program (2017BT01X137).

Conflicts of interest

All authors declared that there are no conflicts of interest.

Ethical approval and consent to participate

Not applicable.

Consent for publication

Not applicable.

Copyright

© The Author(s) 2022.

REFERENCES

1. Liu G, Molokeev MS, Xia Z. Structural rigidity control toward Cr³⁺-based broadband near-infrared luminescence with enhanced thermal stability. *Chem Mater* 2022;34:1376-84. DOI
2. Li J, Cui D, Huang J, et al. Organic semiconducting pro-nanostimulants for near-infrared photoactivatable cancer immunotherapy. *Angew Chem Int Ed Engl* 2019;58:12680-7. DOI PubMed
3. Zhang L, Wang D, Yang K, et al. Mitochondria-targeted artificial “nano-rbcs” for amplified synergistic cancer phototherapy by a single NIR irradiation. *Adv Sci (Weinh)* 2018;5:1800049. DOI PubMed PMC
4. Zou X, Wang X, Zhang H, et al. A highly efficient and suitable spectral profile Cr³⁺-doped garnet near-infrared emitting phosphor for regulating photomorphogenesis of plants. *Chem Eng J* 2022;428:132003. DOI
5. Liu D, Li G, Dang P, et al. Simultaneous broadening and enhancement of Cr³⁺ photoluminescence in LiIn₂SbO₆ by chemical unit cosubstitution: night-vision and near-infrared spectroscopy detection applications. *Angew Chem Int Ed Engl* 2021;60:14644-9. DOI PubMed
6. Nguyen DT, Baek NR, Pham TD, Park KR. Presentation attack detection for iris recognition system using NIR camera sensor. *Sensors (Basel)* 2018;18:1315. DOI PubMed PMC
7. Rajendran V, Chang H, Liu R. Recent progress on broadband near-infrared phosphors-converted light emitting diodes for future miniature spectrometers. *Opt Mater* 2019;1:100011. DOI
8. Zhang Y, Qiao J. Near-infrared emitting iridium complexes: molecular design, photophysical properties, and related applications. *iScience* 2021;24:102858. DOI PubMed PMC
9. Lukovic M, Lukovic V, Belca I, Kasalica B, Stanimirovic I, Vicic M. LED-based vis-NIR spectrally tunable light source - the optimization algorithm. *J Eur Opt Soc -Rapid Publ* 2016;12. DOI
10. Liu H, Zhong H, Zheng F, et al. Near-infrared lead chalcogenide quantum dots: synthesis and applications in light emitting diodes*. *Chin Phys B* 2019;28:128504. DOI
11. Liu G, Hu T, Molokeev MS, Xia Z. Li/Na substitution and Yb³⁺ co-doping enabling tunable near-infrared emission in LiIn₂SbO₆:Cr³⁺ phosphors for light-emitting diodes. *iScience* 2021;24:102250. DOI PubMed PMC
12. Qiao J, Zhou G, Zhou Y, Zhang Q, Xia Z. Divalent europium-doped near-infrared-emitting phosphor for light-emitting diodes. *Nat Commun* 2019;10:5267. DOI PubMed PMC
13. Dai D, Wang Z, Xing Z, et al. Broad band emission near-infrared material Mg₃Ga₂GeO₈:Cr³⁺: substitution of Ga-In, structural modification, luminescence property and application for high efficiency LED. *J Alloys Compd* 2019;806:926-38. DOI
14. Berezovskaya I, Dotsenko V, Voloshinovskii A, Smola S. Near infrared emission of Eu²⁺ ions in Ca₃Sc₂Si₃O₁₂. *Chem Phys Lett* 2013;585:11-4. DOI
15. Qiao J, Zhang S, Zhou X, Chen W, Gautier R, Xia Z. Near-infrared light-emitting diodes utilizing a Europium-activated calcium oxide phosphor with external quantum efficiency of up to 54.7%. *Adv Mater* 2022;34:e2201887. DOI PubMed
16. Xiong PX, Li YY, Peng MY. Recent advances in super broad infrared luminescence bismuth-doped crystals. *iScience* 2020;23:101578. DOI PubMed PMC
17. Matuszewska C, Marciniak L. The influence of host material on NIR II and NIR III emitting Ni²⁺-based luminescent thermometers in ATiO₃: Ni²⁺ (A = Sr, Ca, Mg, Ba) nanocrystals. *J Lumin* 2020;223:117221. DOI
18. Du J, Poelman D. Near-infrared persistent luminescence in Mn⁴⁺ doped perovskite type solid solutions. *Ceram Int* 2019;45:8345-53. DOI
19. Nie W, Yao L, Chen G, et al. A novel Cr³⁺-doped Lu₂CaMg₂Si₃O₁₂ garnet phosphor with broadband emission for near-infrared applications. *Dalton Trans* 2021;50:8446-56. DOI PubMed
20. Nie W, Li Y, Zuo J, et al. Cr³⁺-activated Na₃X₂Li₃F₁₂ (X = Al, Ga, or In) garnet phosphors with broadband NIR emission and high luminescence efficiency for potential biomedical application. *J Mater Chem C* 2021;9:15230-41. DOI
21. You L, Tian R, Zhou T, Xie R. Broadband near-infrared phosphor BaMgAl₁₀O₁₇:Cr³⁺ realized by crystallographic site engineering. *Chem Eng J* 2021;417:129224. DOI
22. Zeng H, Zhou T, Wang L, Xie R. Two-site occupation for exploring ultra-broadband near-infrared phosphor-double-perovskite La₂MgZrO₆:Cr³⁺. *Chem Mater* 2019;31:5245-53. DOI
23. Yan W, Liu F, Lu YY, Wang XJ, Yin M, Pan Z. Near infrared long-persistent phosphorescence in La₃Ga₅GeO₁₄:Cr³⁺ phosphor. *Opt Express* 2010;18:20215-21. DOI PubMed
24. Xu X, Shao Q, Yao L, Dong Y, Jiang J. Highly efficient and thermally stable Cr³⁺-activated silicate phosphors for broadband near-infrared LED applications. *Chem Eng J* 2020;383:123108. DOI
25. Huang D, Zhu H, Deng Z, et al. A highly efficient and thermally stable broadband Cr³⁺-activated double borate phosphor for near-infrared light-emitting diodes. *J Mater Chem C* 2021;9:164-72. DOI
26. Lin Q, Wang Q, Liao M, et al. Trivalent chromium ions doped fluorides with both broad emission bandwidth and excellent luminescence thermal stability. *ACS Appl Mater Interfaces* 2021;13:18274-82. DOI PubMed
27. Bindhu A, Naseemabevi JI, Ganesapotti S. Distortion and energy transfer assisted tunability in garnet phosphors. *Crit Rev Solid*

- State Mater Sci* 2022;47:621-64. DOI
28. Jia Z, Yuan C, Liu Y, et al. Strategies to approach high performance in Cr³⁺-doped phosphors for high-power NIR-LED light sources. *Light Sci Appl* 2020;9:86. DOI PubMed PMC
 29. Basore ET, Xiao W, Liu X, Wu J, Qiu J. Broadband near-infrared garnet phosphors with near-unity internal quantum efficiency. *Adv Optical Mater* 2020;8:2000296. DOI
 30. Mao N, Liu S, Song Z, Yu Y, Liu Q. A broadband near-infrared phosphor Ca₃Y₂Ge₃O₁₂:Cr³⁺ with garnet structure. *J Alloys Comp* 2021;863:158699. DOI
 31. Meng X, Zhang X, Shi X, et al. Designing a super broadband near infrared material Mg₃Y₂Ge₃O₁₂:Cr³⁺ using cation inversion for future light sources. *RSC Adv* 2020;10:19106-16. DOI PubMed PMC
 32. Dumesso MU, Xiao W, Zheng G, et al. Efficient, stable, and ultra-broadband near-infrared garnet phosphors for miniaturized optical applications. *Adv Opt Mater* 2022;10:2200676. DOI
 33. Zhou JY, Zhuo Y, Du F, et al. Efficient and tunable luminescence in Ga_{2-x}In_xO₃:Cr³⁺ for near-infrared imaging. *ACS Appl Mater Interf* 2021;13:31835-42. DOI PubMed
 34. Xia Z, Ma C, Molokeev MS, Liu Q, Rickert K, Poeppelmeier KR. Chemical unit cosubstitution and tuning of photoluminescence in the Ca₂(Al_{1-x}Mg_x)(Al_{1-x}Si_{1+x})O₇:Eu²⁺ phosphor. *J Am Chem Soc* 2015;137:12494-7. DOI PubMed
 35. Shannon RD. Revised effective ionic radii and systematic studies of interatomic distances in halides and chalcogenides. *Acta Cryst A* 1976;32:751-67. DOI
 36. Zhang L, Wang D, Hao Z, et al. Cr³⁺-Doped broadband NIR garnet phosphor with enhanced luminescence and its application in NIR spectroscopy. *Adv Opt Mater* 2019;7:1900185. DOI
 37. Tanabe Y, Sugano S. On the absorption spectra of complex ions II. *J Phys Soc Jpn* 1954;5:766-79. DOI
 38. Mao M, Zhou T, Zeng H, et al. Broadband near-infrared (NIR) emission realized by the crystal-field engineering of Y_{3-x}Ca_xAl_{5-x}Si_xO₁₂:Cr³⁺ (x = 0-2.0) garnet phosphors. *J Mater Chem C* 2020;8:1981-8. DOI
 39. Zhang S, Qiu B, Li Z, et al. Achieving high quantum efficiency independent on luminescence center through sub-lattice cage engineering. *Chem Eng J* 2021;426:130734. DOI
 40. Lian H, Li Y, Sharafudeen K, et al. Highly thermotolerant metal halide perovskite solids. *Adv Mater* 2020;32:e2002495. DOI PubMed
 41. Malysa B, Meijerink A, Jüstel T. Temperature dependent Cr³⁺ photoluminescence in garnets of the type X₃Sc₂Ga₃O₁₂ (X = Lu, Y, Gd, La). *J Lumin* 2018;202:523-31. DOI
 42. Kayanuma Y, Noba K. On the line shape of phonon side-band in photo-absorption of localized centers. *J Phys Soc Jpn* 1999;68:1061-1061. DOI
 43. Tang F, Su Z, Ye H, et al. A set of manganese ion activated fluoride phosphors (A₂BF₆Mn⁴⁺, A = K, Na, B = Si, Ge, Ti): synthesis below 0 °C and efficient room-temperature photoluminescence. *J Mater Chem C* 2016;4:9561-8. DOI
 44. Kitzmann WR, Moll J, Heinze K. Spin-flip luminescence. *Photochem Photobiol Sci* 2022;21:1309-31. DOI PubMed
 45. Macfarlane P, Han T, Henderson B, Kaminskii A. Cr³⁺ luminescence in calcium and strontium gallogermanate. *Opt Mater* 1994;3:15-24. DOI